Interstellar catalysts and the PAH universe

Campisi, D.

Citation

Campisi, D. (2021, September 14). *Interstellar catalysts and the PAH universe*. Retrieved from https://hdl.handle.net/1887/3210124

Author: Campisi, D.
Title: Interstellar catalysts and the PAH universe
Issue Date: 2021-09-14

CHAPTER 5

ADSORPTION OF PAHS AND C_{60} ONTO FORSTERITE: C-H BOND ACTIVATION BY THE SCHOTTKY VACANCY

D. Campisi, Thanja Lamberts, Nelson Y. Dzade, Rocco Martinazzo, Inge Loes ten Kate, and Alexander G. G. M. Tielens, **2021**, submitted

Abstract. Understanding how to break catalytically the C-H bond of aromatic molecules such as polycyclic aromatic hydrocarbons (PAHs) is the first step in converting these species into a variety of organic molecules. This is currently a big challenge and subject of study in catalysis, surface science, organic chemistry, astrochemistry, and planetary science. In the latter, the study of the breakdown reaction of PAHs is important to understand their link with the prebiotic molecules of regions of star and planet formation. Moreover, forsterite is a mineral abundant on our planet and aroused interest as a cheap and safe alternative to synthetic catalysts.

In this work, we employed a periodic DFT-D4 approach to study the surface phenomena of a sample of polycyclic aromatic hydrocarbons (naphthalene, anthracene, fluoranthene, pyrene, coronene, benzocoronene) and fullerene (C_{60}) on the [010] forsterite surface and its defective surfaces for their implication in catalysis and astrochemistry. The defects modeled onto the forsterite surfaces are Fe, Ni-doped surfaces and MgO Schottky vacancy. These defects have shown higher stability when located on the surface layer of the forsterite slab model. PAHs adsorb on the pristine, Fe, and Ni-doped forsterite surfaces with geometrical structures close to planarity. The adsorption of PAHs and C_{60} on the Fe-doped forsterite surface is stronger with respect to the pristine and Ni-doped surface. On these surfaces, PAHs adsorbed with binding energies in a range between about 1 and 2.6 eV. The binding energy of PAHs adsorbed on MgO Schottky forsterite vacancy surface is in the range of about 2-3.5 eV. The binding energy is influenced by the number of contact points (orbital interactions between the carbon atoms and Mg, Fe, and Ni atoms on the surface), which depend on the PAH surface area. The larger is the area, the larger is the number of contact points.

The MgO Schottky vacancy has shown different reactivity based on the orientation of the PAH approaching the surface. Parallel adsorption on the MgO Schottky forsterite vacancy surface leads to the chemisorption of the molecule with the formation of stable covalent C-Si and C-O bonds. On the vacancy surface, anthracene has higher binding energy with respect to the other PAHs due to the presence of perfect $\widehat{COO}$ 109° and $\widehat{SiOO}$ 120° angles in agreement with sp^3 and sp^2 hybridized carbon atoms respectively, whereas the other PAHs diverge from this value. Pyrene and coronene do not form covalent bonds when adsorbed onto the MgO Schottky vacancy. Furthermore, the large surface area of coronene causes the formation of vacancy reconstruction during the adsorption process. Finally, fullerene benefits from the chemisorption on the vacancy surface due to the covalent bond formation that stabilizes the buckyball structure.

Perpendicular orientation of the PAH with respect to the vacancy surface leads to the catalytic breaking of the aromatic C-H bond via a barrierless reaction. With reaction energies between -3.2 and -5.3 eV, perpendicular adsorption is more favourable than the parallel adsorption. Spin density isosurfaces and Voronoi charge analysis show that C-H dissociation is promoted by electron donation from the vacancy to the PAH. As a result of the undercoordinated Si and O atoms, the vacancy acts as a frustrated Lewis pair catalyst. Therefore, MgO Schottky vacancy [010] forsterite surface proved to have potential catalytic activity for the activation of C-H bond breaking in aromatic molecules.

5.1. Introduction

The study of the reactivity of organic molecules as feedstock for the formation of precursors of complex molecular species is the focus of organic chemistry, material science, catalysis, astrochemistry, and planetary science.[8,115,249,250] The orbital interaction of an sp^2 carbon with an s orbital of a hydrogen atom forms a strong C-H bond with bonding energy of about 4.6 eV that we can find in aromatic species such as benzene[251] and polycyclic aromatic hydrocarbons (PAHs).[41] Shedding light on the activation of the aromatic C-H bond is the first step to understand the reactivity of inert species such as PAHs and how to use them as catalytic materials in organic synthesis.[252]

PAHs lock up about 20% of carbon in the universe, whereas 80% is locked up in other species. PAHs might be linked to other organic molecules since they can act as carbon feedstock and, therefore, studying their reactivity is also important to understand the chemical evolution of our universe.[8]

Finding a natural material that is able to activate and catalyze the C-H bond breaking of aromatic species is still a big challenge due to their high bond energy and their high stability. Synthetic and pollutant transition metal catalysts such as Wilkinson's (rhodium-based catalysts),[253] palladium,[254,255] and iridium catalysts[256] are able to break the aromatic C-H bond. However, these catalysts are harmful to human health and moreover very rare and therefore very expensive. Recently metal-free catalysts such as Frustrated Lewis Pairs[257] (FLPs), formed by a Lewis acid and bases that cannot bind together due to steric hindrances, have been studied since they can activate aromatic hydrocarbons.[258]

Mineral-bearing materials are organized periodic systems and have been considered as a cheap and safe alternative to synthetic catalysts.[259] In fact, mineral surfaces have active inorganic interfaces that can host molecular species and possibly activate them.[203] Even though minerals might act as catalysts, they cannot be regenerated during the catalytic cycle (reaction cycle in which a catalyst is partaking). They catalyze processes that are thermodynamically favourable but kinetically hindered by high energy barriers.[260]

Forsterite (Mg_2SiO_4) is one of the most abundant olivinic minerals available on Earth and in space.[46,261] Experimental studies have reported the potential catalytic role of forsterite and Fe-doped forsterite for the conversion of methanol to olefine and PAHs.[262,263] However, theoretical and mechanistic studies on the catalytic activity of forsterite are currently lacking. Only a few studies have addressed the interaction of organic species with a forsterite surface using first-principle methods.[12,218,219]

In this work, we use periodic density functional theory (DFT) along with the Grimme's D4 method[222] (DFT-D4), to study the adsorption and C-H activation of PAHs (naphthalene, anthracene, fluoranthene, pyrene, coronene and benzocoronene) on the most stable [010] forsterite surface ([010]-fo).[12,216,217,261] In space, forsterite is a potential catalyst and, therefore, might be used to promote the conversion of PAHs into other organic species. Along with the pristine [010]-fo surface, we also study defective surfaces of [010] forsterite.[236] Specifically, we modeled the [010]-fo with a single Mg atom replaced by a Fe atom (Fe-[010]-fo),[37,213] by a Ni atom (Ni-[010]-fo)[12] as well as by a MgO-Schottky vacancy (V_{MgO}-[010]-fo).[264] Defects are ubiquitous, at different concentrations, in all crystalline mineral structures. They are often promoted by the radiation of isotopic decay, or by high temperatures during the crystal growth, and they are classified as bulk, planar, line, and point defects.[265] A small amount of Fe and Ni in olivine is generally present,[236,238,239] whereas the presence of MgO-Schottky vacancy might have been the result of the reaction of olivine with a small amount of water.[62]

We also include in this study the adsorption of C_{60} as this molecule is abundant in space.[266,267] We analyze geometrical parameters and binding energies for the adsorption of PAHs and C_{60} as well as the energy barriers and the electronic structure associated with the C-H dissociation of PAHs on the vacancy forsterite surface. This study is the starting point to understand the chemistry of aromatic molecules in interstellar space and on solar system bodies as well as for the potential role of minerals as selective catalysts for industrial applications.

5.2. Theoretical Methods

Forsterite and PAH Structures. In this study, we model the crystalline non-polar [010]-fo surface ($Mg_{96}O_{192}Si_{48}$) and its defective surfaces under dry conditions, shown in Fig. 5.1. The present theoretical models are used to study forsterite material as an important component of interstellar dust grains, asteroids, meteorites[46] as well as for its potential use as a catalyst.[262] All models have a 19 Å x 17.94 Å x 35.20 Å ($\alpha = \beta = \gamma = 90°$) supercell (4 x 3 x 1) with a slab thickness of 9.25 Å. The [010] slab surfaces were generated cutting the optimized bulk of forsterite from a prior study[12] using METADISE code.[220] The bottom layers (layers with a thickness of about 4 Å) have been constrained during the whole optimization procedure. The presence of defects has proved to increase the reactivity and catalytic activity of several materials.[16,60,268] Therefore, we decided to model the defective surfaces of [010]-fo by substituting, using chemical intuition, a transition metal (*e.g.*, Fe and Ni for this work) for an undercoordinated Mg atom from the surface and optimizing the resulting slab model. Furthermore, V_{MgO}-[010]-fo is created by removing a MgO unit from the [010]-fo surface, again followed by a reoptimization of the slab.

The PAHs taken into consideration in this study, are naphthalene, anthracene, pyrene, fluoranthene, coronene, benzocoronene and fullerene.

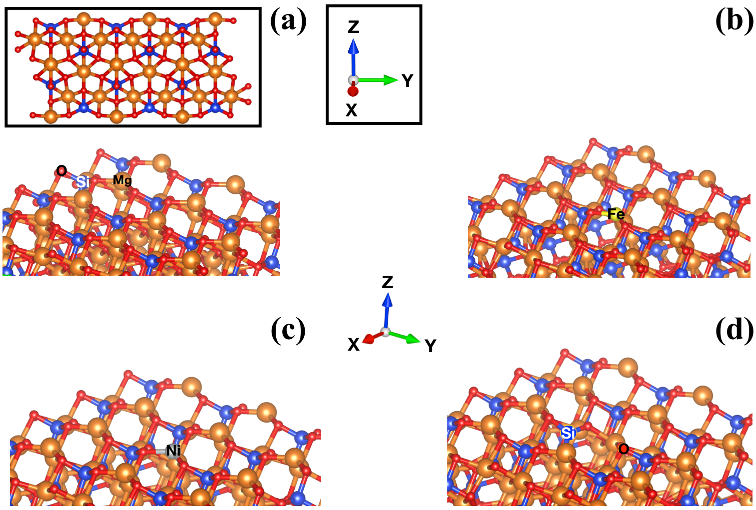

Figure 5.1: Optimized slab models of [010] forsterite at two different orientations: (a) [010]-fo, (b) Fe-[010]-fo, (c) Ni-[010]-fo and (d) V_{MgO}-[010]-fo (the location of the vacancy is indicated by the Si and O labels reported on the corresponding undercoordinated atoms). The vacuum region is located along the z axis and the atomic labels of the corresponding atoms are reported.

These species (Fig. 5.3 as well as Fig. 5.14 - 5.19 in the Appendix) are characterized by honeycomb structures of fused hexagonal carbon rings bound with hydrogen atoms on their edges. Fluoranthene is the only PAHs with a 5-membered ring. The fullerene, C_{60}, is characterized by a sperical shape (buckyball) with hexagonal and pentagonal rings bound together forming [6,6] and [5,6] ring junctions (Fig. 5.19 in the Appendix) which are bridge carbons atoms of two hexagonal rings, and hexagonal-pentagonal rings, respectively. The gas phase model of PAHs has been optimized in a cubic unit cell with sides of 15 Å.

Calculation Setup. The slab models were optimized using periodic density functional theory implemented in the SIESTA code[98] that makes use of localized atomic orbitals basis sets (LCAO). The details of the method have been described in a prior work[12] and are summarized here:
We employ the Perdew, Becke, and Ernzerhof[210] (PBE) exchange-correlation functionals along with DZP basis set using core pseudopotentials and setting the radii of split valence type for the hydrogen atoms to 0.5. The counterpoise correction[100,101] (CP) is taken into account for all calculations to correct for the basis set superposition error (BSSE). We conventionally labeled the counterpoise corrected basis sets as CP-DZP, as reported in our previous work.[12] The dispersion energy is taken into ac-

count a posteriori, on the optimized geometry at PBE/DZP level, employing Grimme's DFT-D4 code.[206,221,222] The Brillouin zone is sampled using 2 x 2 x 1 Monkhorst–Pack's[102] k-points for all surfaces with a unit cell of 18.996 Å x 17.938 Å and 1x1x1 Monkhorst–Pack's k-points for the gas phase models (reagents). The mesh cutoff is set to 200 Ry (see Appendix of chapter 4). All calculations are run with the unrestricted formalism and convergence is reached when the forces are lower than 0.01 eV Å $^{-1}$. All structures are optimized using the limited-memory Broyden–Fletcher–Goldfarb–Shanno (L-BFGS) algorithm.[269] An electric field along the z-axis is set to override the resulting dipole moment along the z-axis of the slabs during the optimization procedure. In a prior study,[12] PBE-D4/CP-DZP was proven to be a robust theory level to study the interaction of aromatic molecules on mineral surfaces.

We analyzed the electronic mechanism of the vacancy surface with the spin density isosurfaces and the charge analysis population based on Voronoi scheme that proved to be more accurate than Mullikan and Bader schemes.[270] These techniques allow us to define the spin-up and spin-down population (spin density) of each atom as well as the electronic donation and reception between the atoms (partial atomic charges). The spin density and charge analysis have been calculated at the PBE + U level of theory with a single point calculation using TZP on the optimized DZP geometry with supplementary 4 x 4 x 1 Monkhorst–Pack's k-points. The Hubbard U value, using the LDA + U method,[226] is set to 15.3 eV to describe the strong on-site Coulomb interaction of the localized electrons of the 2p orbitals of the oxygen atoms to reproduce the experimental band-gap (8.4 eV).[227] A threshold tolerance of 10^{-2} and a tolerance population of $4x10^{-4}$ is selected for the LDA + U method. The radii for the split-valence type of TZP for all atoms, excluded hydrogen, are set up to be 0.30. The reaction barriers (*e.g.*, the characterization of a saddle point) and the minimum energy path are calculated using the climbing-image nudged elastic band method[271] (CI-NEB) implemented in the atomistic simulation environment[272,273] (ASE) python module employing SIESTA as a calculator. The minimum energy path is optimized linearly interpolating the reagent and the product by six images. Each image can be thought of as a representation along the reaction path with all images interconnected by springs. The optimization focuses on finding the lowest energy possible for each image, and the maximum one only for one image, while maintaining the constraint that they are equally spaced with respect to neighboring images. Note that after optimizing the CI-NEB path, the energies of the images represent the minimum energy path from the initial to the final geometry. The path is optimized using the Fast Inertial Relaxation Engine (FIRE)[274] algorithm that provides robust results compared to Quasi-Newton methods.[275] The spring constant is set to 0.1 eV/Å and the six images between the reagent and the product are considered optimized when the forces are lower than 0.025 eV/Å .

In this work, the binding energy (E_{bind}) is defined as:

$$E_{\text{bind}} = [(E_{\text{mol}} + E_{\text{slab}}) - E_{\text{mol-slab}}] \tag{5.1}$$

E_{mol} is the energy of the optimized molecule in the gas phase, E_{slab} is the energy of the optimized forsterite slab and $E_{\text{mol-slab}}$ is the energy of the optimized adsorbed molecule on the forsterite slab. Positive binding energy values show endoergic adsorption processes.

The reaction energy (E_{react}) is defined as:

$$E_{\text{react}} = [(E_{\text{product}} - (E_{\text{slab}} + E_{\text{mol}})] \tag{5.2}$$

E_{product} is the energy of the optimized product. For definition, E_{react} = -E_{bind}. Therefore, negative values of E_{react} shows favourable and exoergic processes.

We define contact points (C.P.) as the sum of orbital interactions between the p orbital of a carbon atom with the 3p orbital of a Mg atom, 3d orbital of Fe and Ni atoms.

The surface area of each PAHs is calculated as the sum of the area of the single hexagons and/or pentagons using the carbon backbone, *i.e.*, excluding the bound hydrogens.

5.3. Results and Discussion

5.3.1. Structure of the [010] Forsterite Surfaces

The [010]-fo surfaces are constituted by an orthorhombic structure with Pbnm space group and it differs from the bulk because of the presence of under-coordinated Mg atoms bound with three neighboring oxygen atoms on the external layer that faces the vacuum region.

The surface structure of [010]-fo is characterized by undercoordinated Mg atoms (M1) shown in Fig. 5.2 and fully coordinated Mg atoms (M2) located in the underlying layer. The Si (Si1) atoms on the surface are fully coordinated (tetrahedral structures). The bond distances, only for the atoms located on the surface, are reported in the table included in Fig. 5.2 and show Mg-O and Si-O distances ranging between 1.63 and 1.90 Å. Mg, O and Si atoms, on the surface, form zig-zag edges following an alternating unit scheme: -O-Si-O-Mg-O-. The Mg-O bond lengths of the under-coordinated Mg atoms on the surface (M1) are shorter than those of the octahedral Mg-O (M2-O2) with a bond distance that ranges between 2-2.16 Å. All calculated bond lengths are in agreement with the study carried out by Navarro-Ruiz *et al.*[213] using LCAO methods and by Brodholt using plane wave methods.[276]

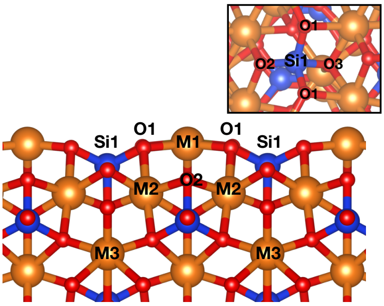

	[010]-fo (M=Mg)	Fe-[010]-fo (M=Fe)	Ni-[010]-fo (M=Ni)	V_{MgO}-[010]-fo
d(M1-O1)	1.86	1.89	1.88	
d(M1-O2)	1.90	1.96	1.93	
d(Si1-O1)	1.67	1.67	1.67	1.62
d(Si1-O2)	1.63	1.62	1.62	1.57
d(Si1-O3)	1.73	1.73	1.73	1.63
$\widehat{O1M1O1}$	123	126	120	
$\widehat{O1Si1O1}$	109	107	108	

Figure 5.2: Side-view figure that shows the labels of the atomic positions of the [010]-fo forsterite. M shows the location of an Mg, Fe, Ni atoms, or MgO vacancy. The table reports distances (d), in Angstrom (Å), and angles ($\frown$), in degree (°), of the atoms reported in the above figure.

We also studied the presence of point defects on the [010]-fo surface, shown in Fig. 5.1 (b). The Fe-[010]-fo surface is characterized by an undercoordinated Fe^{2+} atom bound to three oxygen atoms. When the Fe is located in the M1 site, it is more stable by 0.30 eV with respect to the M2 site and 0.22 eV with respect to the M3 site. Hence, M1 is the preferred site (Fig. 5.2). The table reported in Fig. 5.2 shows the bond distances and angles of the Fe-[010]-fo that are in close agreement with the geometrical parameters of the pristine surface.

Along with Fe-[010]-fo, we considered the presence of undercoordinated Ni as a point defect on the surface, Ni-[010]-fo (Fig. 5.1 (c)). The location of the Ni point defect in the M1 site is slightly more stable by about 0.04 and 0.01 eV compared to the M2 and M3, respectively. However, this difference is not significant considering the accuracy of the functional.[12] Once the transition metal coordinates with an aromatic molecule such as naphthalene, the Ni point defect in the M1 site is stabilized by 0.30 eV and 1.61 eV with respect to M2 and M3, respectively. The table in Fig. 5.2 shows bond distances and angles for the Ni-[010]-fo which are in close agreement with Fe-[010]-fo and [010]-fo. Overall, the presence of transition metals does not significantly change the forsterite structure compared to the pristine [010]-fo structure.

Another type of defect occurring in crystalline structures is the MgO

	Surface Area (Å^2)
Naphthalene	10.18
Anthracene	15.28
Fluoranthene	18.34
Pyrene	20.37
Coronene	35.64
Benzocoronene	40.73
Forsterite surfaces	340.74

Table 5.1: Surface area of PAHs and the [010] forsterite surfaces ([010]-fo, Fe-[010]-fo, Ni-[010]-fo, V_{MgO}-[010]-fo) optimized in this study. The average sizes of the hexagons and pentagons are 1.40 Å which is the distance of a single C-C bond.

Schottky defect. This defect is formed when a cation-anion pair is removed, resulting in a vacancy.[277] The energy required to form the Schottky MgO vacancy defect is about 7 eV.[62] For comparison, SiO_2 vacancies are less favorable since the formation energy is about 20 eV.[62] The presence of the Schottky MgO vacancy (V_{MgO}-[010]-fo), shown in Fig. 5.1 (d), causes an interruption of the zigzag units resulting in the formation of a SiO_3^{2-} unit and O atoms that bridge an Mg and Si atom. The absence of an Mg atom does not allow the formation of a bond between the two distant Si and O atoms on the surface. The distance between these not bound Si and O atoms, the two labeled atoms in Fig. 5.1 (d), in the vacancy is about 5.12 Å causing the formation of a cavity. The table in Fig. 5.2 shows that the Si-O distances are slightly shorter compared to the other surfaces. Instead, the O atom that lacks of a neighbour Si atom because of the vacancy (Fig. 5.1 (d)), binds with a second neighbour Si (Si1) which has a distance of 1.61 Å and 1.97 Å with the Mg located in the M2 site. Therefore, the cavity formation causes a bond length reorganization to compensate for the absence of an Mg atom. The MgO vacancy is more stable when located on the surface in the M1 site by about 2.90 and 4.94 eV with respect to the M2 and M3 sites, respectively. Hence, M1 is the most favorable site for all the three defects considered in this study.

5.3.2. Interaction of PAHs and C_{60} with [010] forsterite

Structural Analysis. Previous theoretical studies have shown that forsterite strongly binds with aromatic molecules on its surfaces.[12,218,219] Therefore, we have selected a sample of PAHs that span a range in surface area (Table 5.1) and that contain catacondensed PAHs (*e.g.*, the acenes naphthalene and anthracene), pericondensed PAHs (pyrene and coronene), and irregular PAHs (benzocoronene). In addition, we also selected the non-alternant aromatic species fluoranthene and fullerene. The skeleton structure of the mentioned PAHs is reported in Fig. 5.3.

We optimized all structures for a parallel adsorption of the molecular

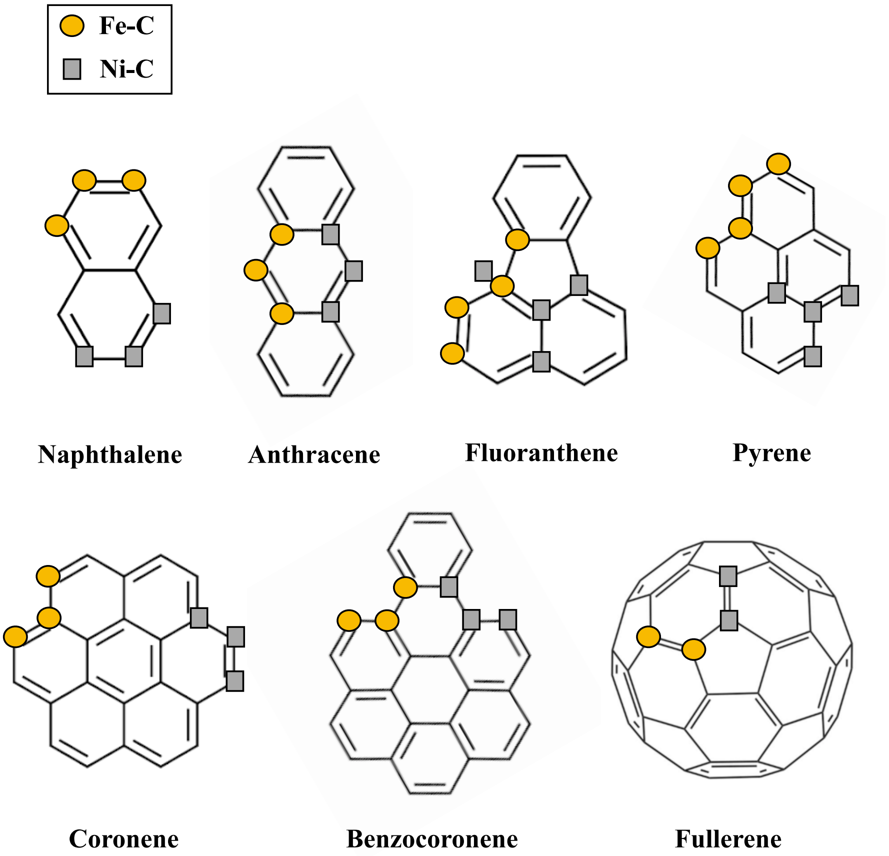

Figure 5.3: The skeleton structure of PAHs and the location of carbon-transition metal interactions less than 3 Å (see Appendix), on the PAH structure, when they adsorb on the Fe and Ni-[010]-fo. The legend shows the symbol related to C-Fe (circles) and C-Ni (squares) interactions.

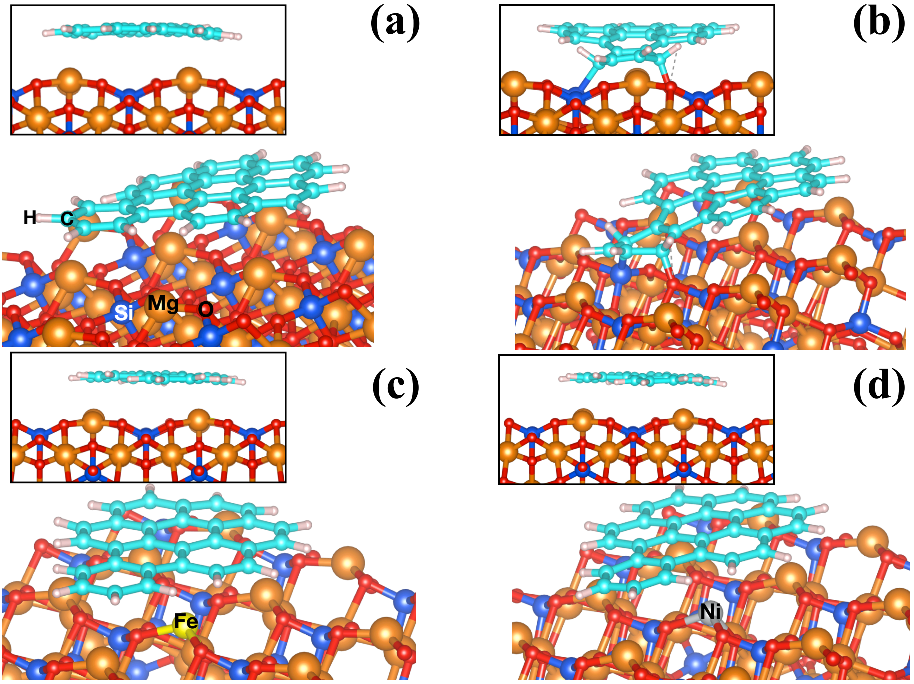

Figure 5.4: Side views using two different perspectives (second prospective in thumbnail) of the optimized geometries of benzocoronene adsorbed on (a) [010]-fo, (b) V_{MgO}-[010]-fo, (c) Fe-[010]-fo and (d) Ni-[010]-fo. Atomic labels are reported on the corresponding atoms.

plane with respect to the surface. The adsorption of PAHs on the [010] forsterite surfaces causes a slight deviation of the PAH structure from their planarity (Fig. 5.4). This is in line with the average dihedral angles of the carbon atoms of the PAH skeleton, reported in table 5.2. The average dihedral angles do not show characteristic planar structures of 180°. With the exception of pyrene, PAH adsorption on [010]-fo and Fe-[010] causes a larger deviation from planarity than for Ni-[010]-fo in which the adsorbed molecules have dihedral angles close to 180°. The average angles indicate a perfect 120° characteristic of sp^2 carbons for all PAHs with the exception of fluoranthene. The latter show larger angle deviation from 120° with respect to the other PAHs due to the presence of a 5-membered ring that causes major bending of its structure. The major flexibility due to the presence of a 5-membered ring has been identified also in other materials with PAH-like structures.[60] However, the conformational structure of PAHs on a solid surface, based on the angles and dihedral angles reported in Table 5.2, is close to the perfect planar structure that characterizes them in the gas phase. The conformational structure of the PAHs as well as the fullerene

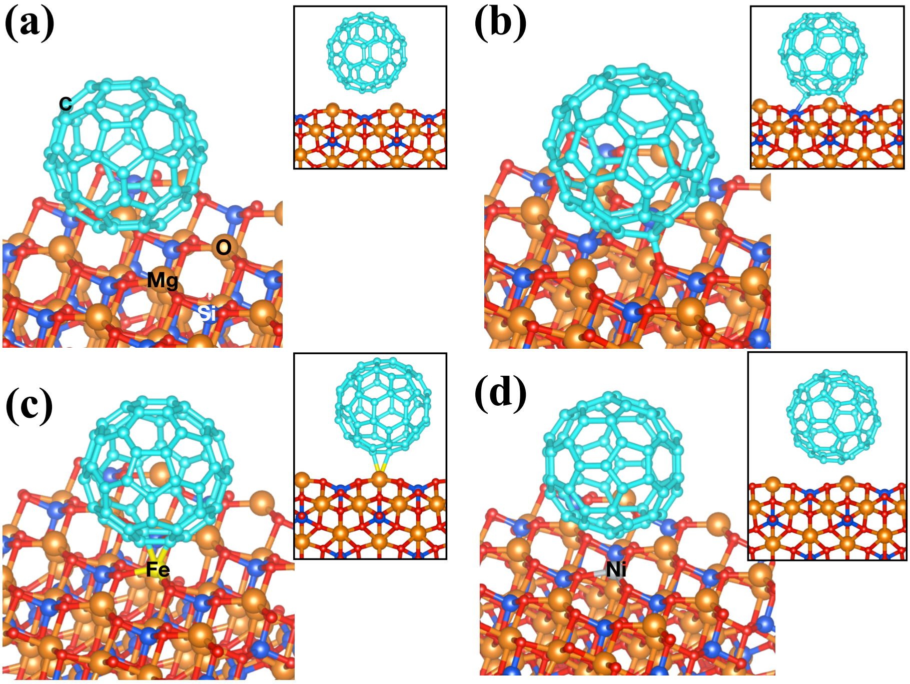

Figure 5.5: Side views using two different perspectives (second prospective in thumbnail) of the optimized geometries of fullerene adsorbed on (a) [010]-fo, (b) Fe-[010]-fo, (c) Ni-[010]-fo and (d) V_{MgO}-[010]-fo. Atomic labels are reported on the corresponding atoms.

on a solid surface, based on the angles and dihedral angles reported in Table 5.2, are very similar to those in the gas phase. Hence, the PAHs adsorbed on the surface have the 120° angles expected for planar PAHs while the fullerene (C_{60}) deviate from this by about 6° as expected for a buckyball-like structure (Fig. 5.5 (a), (c) and (d)).[278]

The larger is the surface area of the PAHs (Table 5.1), the larger is the number of the interaction of the C atoms either with an Mg or transition metal atoms (contact points), as shown in Table 5.2. Pyrene has a larger surface area with respect to fluoranthene. However, the number of contact points in pyrene is lower than fluoranthene. This is due to the more compact structure of the pyrene skeleton with respect to fluoranthene. With the exception of pyrene and fullerene, the number of Mg atoms interacting with carbon atoms at a distance less than 3 Å increases with increasing surface area of the PAH. Therefore, the larger is the surface area, the higher is the number of contact points. Distances larger than 3 Å do not present orbital interactions (see Population Analysis in the Appendix).

Interaction of PAHs and C_{60} with Doped Forsterite. Fig. 5.3 shows

Table 5.2: Geometrical parameters of PAHs adsorbed on forsterite surfaces. Reported the average distance ($\overline{d}$) in Angstrom (Å), average angles ($\overline{Ang.}$) and dihedral angles ($\overline{\Theta}$), in degree (°), number (n) of atoms (C, Mg or M) interacting with each other (*e.g.*, [nC - nMg]) and the number of contact points (C.P.) which is the sum of carbon atoms interacting either with an Mg or transition metal. M is the transition metal (*e.g.*, Fe or Ni) of the corresponding surface (*e.g.*,Fe for Fe-[010]-fo). Missing values show no interaction between the atoms. The average values are calculated from the geometrical parameters reported in the Appendix.

	$\overline{d}$(C-Mg)	$\overline{d}$(C-M)	$\overline{Ang.}$	$\overline{\Theta}$	[nC - nMg]	[nC - nM]	C.P.
Naphthalene:							
[010]-fo[12]	2.61		120.21	176.18	5 - 2		5
Fe-[010]-fo[12]	2.51	2.43	120.02	172.04	2 - 1	3 - 1	5
Ni-[010]-fo[12]	2.64	2.42	120.04	178.14	2 - 1	3 - 1	5
Anthracene:							
[010]-fo	2.65		120.82	173.06	6 - 2		6
Fe-[010]-fo	2.70	2.40	120.47	176.65	3 - 2	3 - 1	6
Ni-[010]-fo	2.73	2.41	120.38	177.05	3 - 2	3 - 1	6
Fluoranthene:							
[010]-fo	2.68		125.34	174.68	7 - 3		7
Fe-[010]-fo	2.62	2.56	125.73	176.99	3 - 2	4 - 1	7
Ni-[010]-fo	2.52	2.62	126.02	177.83	2 - 1	4 - 1	6
Pyrene:							
[010]-fo	2.72		120.79	179.15	5 - 2		5
Fe-[010]-fo	2.64	2.61	121.19	175.30	3 - 1	4 - 1	7
Ni-[010]-fo	2.66	2.50	120.86	177.64	3 - 1	4 - 1	7
Coronene:							
[010]-fo	2.73		120.92	175.63	11 - 4		11
Fe-[010]-fo	2.63	2.51	120.97	174.78	7 - 3	3 - 1	10
Ni-[010]-fo	2.68	2.46	120.80	177.90	5 - 3	3 - 1	8
Benzocoronene:							
[010]-fo[12]	2.71		120.61	176.29	11 - 4		11
Fe-[010]-fo[12]	2.66	2.47	120.46	178.90	8 - 4	3 - 1	11
Ni-[010]-fo[12]	2.67	2.48	120.43	179.18	8 - 4	3 - 1	11
Fullerene:							
[010]-fo	2.74		113.49	139.00	4 - 2		4
Fe-[010]-fo		2.10	106.82	133.63		2 - 1	2
Ni-[010]-fo	2.81	2.09	111.65	143.19	1 - 1	2 - 1	3

the preferred carbon sites of PAHs and fullerene that interact with Fe or Ni on the surface. Naphthalene, anthracene, coronene and benzocoronene have the same number of transition metal interactions, three interactions, located in the edge carbons of the PAHs. Fluoranthene and pyrene have the same number of C-Fe and C-Ni interactions since they are closer in surface area with respect to the other PAHs. However, for fluoranthene and pyrene, we noticed a different behavior of Ni-C interactions since the optimization of the geometry led to a structure in which the inner carbon of these PAHs can interact with Ni atoms at distances smaller than 3 Å (see Geometrical Parameters in the Appendix for details). Instead, fullerene has the same number of Fe-C and Ni-C interactions located in the [6,6] ring junction.

On the transition metal doped surfaces (Fe and Ni-[010]-fo), PAHs do not adsorb with the center of the π-ring as seen for benzene-cation complexes (gas phase configuration) with the same spin configuration of the surfaces (quintet for Fe^{2+} and triplet for Ni^{2+}).[12] The gas phase configuration shows carbon-transition metal (C-M) bond distances of about 2.28 Å for Fe^{2+} and 2.17 Å for Ni^{2+} (values calculated from the optimized geometries reported in a prior study[12] and in agreement with published theoretical studies of Fe-PAH complexes in the gas-phase[279]). The PAHs on forsterite surfaces have, as shown in Table 5.2, C-M bond distances slightly larger with respect to the gas phase configuration. On a regular forsterite surface, the PAH will orient itself on the surface to interact closely with as many Mg atoms as possible. For doped surfaces, binding of PAHs is a competition of a favorable orientation to interact with as many as possible Mg atoms and to optimize the interaction with the transition metal. Table 5.2 summarizes this competition, illustrating that on doped surfaces, the number of C-Mg interactions decreases relative to the pristine surface but that this is compensated for by the interactions with the transition metal. In general, but not always, the number of contact points remains the same. We do note that the difference between the Fe-C and Ni-C bond distances of the PAHs on forsterite surfaces with respect to the gas phase configuration, considering the optimized distance, is about 0.12-0.33 Å for Fe and 0.24-0.45 Å for Ni. Hence, on an Fe-doped surface, PAHs can optimize the Fe-C distance better than on a Ni-doped surface. Fullerene shows smaller (Table 5.2) C-Fe and C-Ni distances than in the PAHs, resulting in a stronger interaction.

Interaction of PAHs and C_{60} with a Vacancy. The geometrical structures of all species adsorbed on V_{MgO}-[010]-fo are reported separately in a table in Fig. 5.6. The vacancy has peculiar structures with respect to the pristine and doped transition metal ones. Specifically, the adsorption of naphthalene, anthracene, fluoranthene, benzocoronene, and fullerene have characteristic $\widehat{O1C1C2}$ angles for the rehybridization of the C atoms of PAHs from sp^2 to sp^3 (about 109°). The C-Si bond has a short distance,

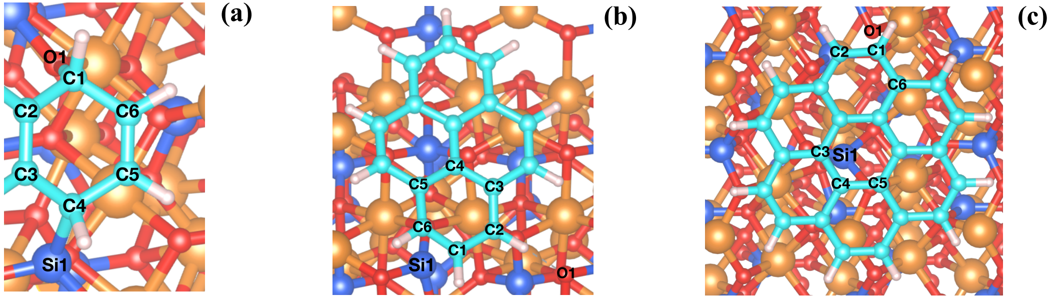

	V_{MgO}-[010]-fo	Naph.	Anth.	Fluora.	Py.	Coro.	Benzo.	C_{60}
d(O1-Si1)	5.12	4.64	4.63	4.66	4.86	5.35	4.62	4.74
d(O1-C1)		1.46	1.45	1.47			1.46	1.44
d(Si1-C5)		1.99	2.00	2.00			2.02	1.99
d(O1-C2)					2.83	2.27		
d(Si1-C1)					2.25			
$\bar{d}$(C-Mg)			2.70	2.83	2.75	2.59	2.64	2.81
$\widehat{O1C1C2}$		111.59	109.16	111.82			112.68	111.59
$\widehat{C6C1C2}$		110.07	110.02	108.72		121.019	110.64	110.07
$\widehat{Si1C4C3}$		118.97	120.36	117.97			116.61	118.97
$\widehat{C5C4C3}$		112.05	112.03	110.57		120.21	112.06	112.05
$\widehat{O1C2C3}$					121.09			
$\widehat{C1C2C3}$					118.30			
$\widehat{Si1C1C6}$					86.68			
$\widehat{C2C1C6}$					119.58			
$\mid \overline{\Theta} \mid$		162.04	161.97	172.25	173.57	176.71	161.57	150.58
C.N. (O1)	2	3	3	3	2	2	3	3
C.N. (Si1)	3	4	4	4	4	4	4	4
$[nC - nMg]$			1 - 1	3 - 2	2 - 1	5 - 3	2 - 1	3 - 1

Figure 5.6: For the PAHs adsorbed on the V_{MgO}-[010]-fo surface we report: A schematic representation (naphthalene, anthracene, fluoranthene, benzocoronene, and fullerene) of the atomic labels of the hexagonal ring chemisorbed with the undercoordinated Si and O (Figure (a)). The same as Figure (a) but for pyrene and coronene (Figure (b) and (c)). A table reporting the average distance ($\bar{d}$) and distance (d) in Angstrom (Å), angles ($\widehat{\ }$) and average dihedral angles ($\mid \overline{\Theta} \mid$), in degree (°), coordination number (C.N.) for the specified atom and the number (n) of atoms (C and Mg) interacting with each other ([nC - nMg]) for the vacancy surface, PAHs and C_{60}. Missing values show no interaction between the atoms. The average values are calculated from the geometrical parameters reported in the Appendix.

about 1.9 Å, and the $\widehat{SiC4C3}$ angles, about 127-133°, are close to the geometrical parameters of silane complexes (about 120°).[280] Therefore the adsorption of these species on the vacancy surface causes the breaking of one aromatic ring (*i.e.*, a chemisorption process). The $\widehat{O1C1C2}$ angles, in the table in Fig. 5.6, show a perfect 109° for anthracene while the other PAHs slightly diverge from this value. Hence, the surface area of anthracene allows a perfect interaction with the vacancy. Pyrene and coronene do not show covalent bond formation. In fact, only species with a terminal aromatic ring with four hydrogen atoms (naphthalene, anthracene, fluoranthene, benzocoronene) and the six-membered ring of fullerene form covalent bonds with the undercoordinated Si and O atoms (see C. N. in the table in Fig. 5.6). This occurs due to their large structural flexibility with respect to more compact structures such as pyrene and coronene. The coordination number of O and Si increases once PAHs adsorb on the vacancy forsterite surface in line with the formation of C-O and C-Si bonds. For the case of pyrene, the molecule binds only with the Si atom, leaving the O atom with a lower coordination number (2) with respect to the adsorption of the other PAHs and C_{60}. However, the Si-C distance, for the case of pyrene, is larger by about 0.25 Å than for the other PAHs chemisorbed on the vacancy. The adsorption structure of pyrene on the vacancy is shown in Fig. 5.6 (b). All species have O-C and Si-C bond distances in good agreement with the average experimental values (1.40 and 1.87 Å).[281]

The distance of undercoordinated Si and O atoms on the vacancy structure is reduced once their coordination is completed by the chemisorption of the PAHs (see O1-Si1 distance in the table reported in Fig. 5.6). However, for the case of coronene, the distance O1-Si1 increases with respect to the non-coordinated surface. Angles and dihedral values of coronene adsorbed on the vacancy do not show the formation of C sp^3, but a quasi-planar structure in agreement with the adsorption on the pristine and transition-metal doped surfaces. The coordination number of O and Si of the vacancy, when coronene is adsorbed on it, is completed. Nevertheless, for the case of coronene adsorbed on the vacancy, there is no covalent bond formation, the vacancy enlarged its structure to accommodate the large surface area of coronene which in turn causes the formation of a Si reconstruction as shown in Fig. 5.7. The vacancy reconstruction, caused by the adsorption of coronene on the vacancy, is characterized by the formation of the Si-O bond located in the underlying surface moving the Si atom in between the surface layer and the layer below the surface, completing the coordination of the Si atom. Also, the O atom on the vacancy completes the coordination with a Si located in the underlying surface.

Due to the interaction of the PAHs with the vacancy, the number of Mg atoms interacting with C atoms is much lower with respect to the pristine and metal-doped surfaces, comparing the values between the Table 5.2 and the table reported in Fig. 5.6, respectively.

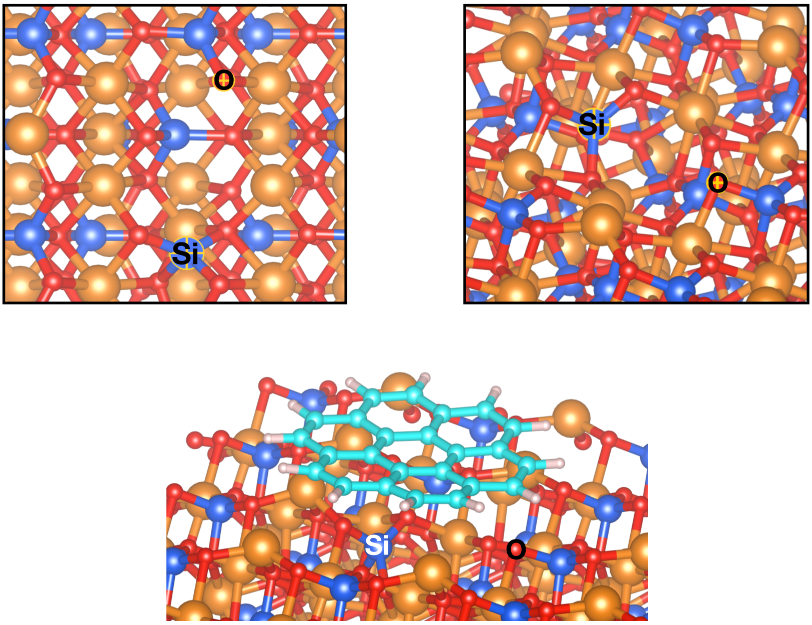

Figure 5.7: Vacancy reconstruction caused by the adsorption of coronene on V_{MgO}-[010]-fo. In thumbnail reported the close-up perspective of the reconstruction. The atomic labels on the corresponding atoms indicate the reconstructed atoms.

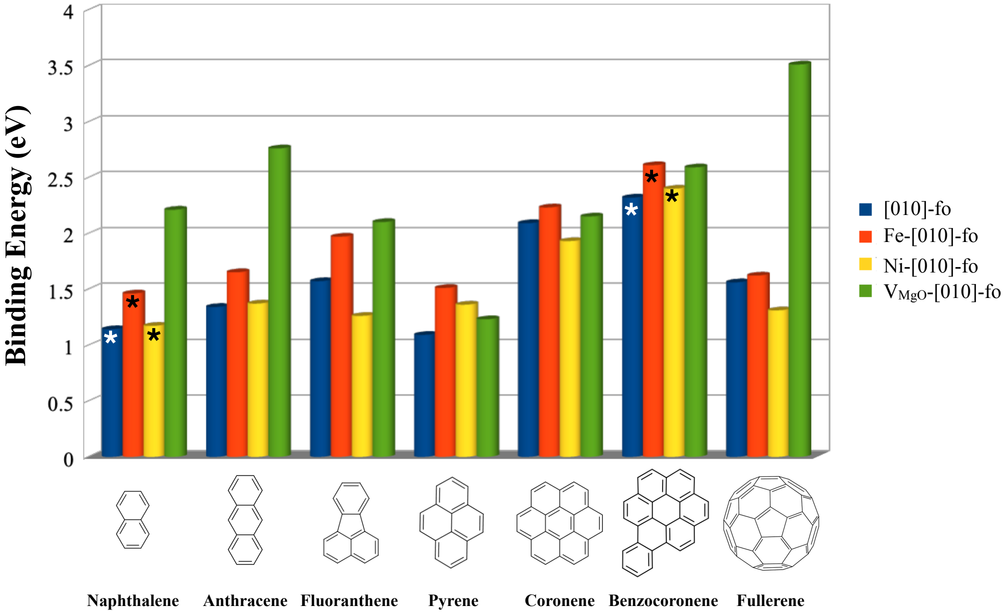

Figure 5.8: Binding energies of the adsorption of PAHs on [010] forsterite surfaces modeled in this study. The surfaces follow the order shown in the legend for all PAHs. Numerical values are reported in the Appendix. The asterisks (*) on the bars show data reported from a prior work.[12]

Binding Energy Analysis. Fig. 5.8 summarizes the binding energies for the PAHs adsorbed on the four different surfaces considered in this study. Disregarding for the moment, the interaction with the Schottky defect, there is a general trend of increasing binding energy with PAH size/surface area but pyrene forms an exception to this. Not surprisingly given its geometry, the fullerene does not adhere to this trend either. The general increase of the binding energy is to be attributed to the increasing number of contact points (see Table 5.2) that is related to the size of the surface area (see Table 5.1). We remind that the larger is the surface, the larger is the number of contact points. Excluding for now the binding energies of the vacancy surface, all PAHs are slightly more stabilized (larger binding energy) on the Fe-[010]-fo with respect to Ni-[010]-fo which is opposite to the adsorption behavior of Fe^{2+} and Ni^{2+} on benzene in the gas-phase (gas phase configuration).[12] As discussed in Structural Analysis section, this reflects subtle geometrical differences in the balance between Mg-PAH and Ni-PAH interactions. PAH adsorption on Fe-doped forsterite shows consistently higher binding energies than on the pure surface, reflecting that PAHs can optimize their interaction on this surface better than

Table 5.3: Binding energies (E_{bind}), angles ($\widehat{\ }$) of PAHs chemisorbed on V_{MgO}-[010]-fo surface.

	E_{bind} (eV)	$\widehat{O1C1C2}$	$\widehat{Si1C4C3}$
Naphthalene	2.21	111.59	118.97
Anthracene	2.76	109.16	120.36
Fluoranthene	2.10	111.82	117.97
Benzocoronene	2.59	112.68	116.61
Fullerene	3.51	111.59	118.97

Table 5.4: Binding energies (E_{bind}), at PBE-D4/CP-DZP and PBE/CP-DZP levels, and dispersion energy (D4) for the interaction of PAHs with V_{MgO}-[010]-fo surface.

	E_{bind}^{PBE-D4} (eV)	E_{bind}^{PBE} (eV)	D4 (eV)
Naphthalene	2.21	1.17	1.05
Anthracene	2.76	1.50	1.25
Fluoranthene	2.10	0.62	1.48
Pyrene	1.23	0.10	1.32
Coronene	2.15	0.55	2.15
Benzocoronene	2.59	0.35	2.30
Fullerene	3.51	1.78	1.74

on a Ni-doped surface. The binding energy trend between Fe and the pristine surface is, instead, in agreement with the gas-phase configuration.[241]

As shown in Fig. 5.8, all molecules bind strongly on the vacancy surface with binding energies larger than 2 eV. We note that anthracene has larger binding energies than naphthalene in line with the reactivity studies conducted by Bonfanti *et al.*[137] and Rasmussen *et al.*[124] Anthracene adsorbs on the vacancy surface with the formation of perfect C-Si and C-O bonds and $\widehat{O1C1C2}$ and $\widehat{Si1C4C3}$ angles of 109° and 120°, respectively. Table 5.3 shows the binding energy of PAHs and fullerene as a function of the $\widehat{O1C1C2}$ and $\widehat{Si1C4C3}$ angles (see labels in Fig. 5.6). Excluding the special case of fullerene, the binding energy of PAHs decreases as a function of the angle deviations from 109° and 120°, for $\widehat{O1C1C2}$ and $\widehat{Si1C4C3}$ respectively. Therefore, antrhacene is the PAH that benefits the most from the adsorption process on the vacancy surface. Fullerene is an exception since it benefits from the formation of covalent bonds with the O and Si atoms on the vacancy and, therefore, from the re-hybridization of the carbon atoms (from tensioned sp^2 to sp^3 carbons)[278] that break the symmetry of the icosahedral structure. Despite that benzocoronene has larger geometrical deviations than other PAHs (see angles in Table 5.3), its binding energy is closer to the anthracene one due to the higher dispersion energy (see Table 5.4). The binding energy of pyrene and coronene deviates with respect to the other PAHs due to their physisorption state (see discussion in Structural Analysis section and the table in Fig. 5.6).

The difference of binding energies between the vacancy surface and the pristine surfaces is much larger for naphthalene, anthracene, and fullerene than for the other PAHs. The smaller number of contact points for naphthalene and anthracene as compared to the other PAHs makes the contribution from the covalent bond formation on the vacancy surface relatively more important. The propensity of fullerenes for addition reactions through the carbons of the 6-membered ring facilitates covalent bond formation on the vacancy surface and results in a relatively high binding energy.

Adsorption Mechanism. In the previous section, we have seen that PAHs strongly bind on the vacancy surface with the formation of C-O and C-Si bonds. In order to evaluate the possible presence of activation barriers associated with the formation of covalent bonds (see Structural Analysis section), we have calculated the minimum energy path employing the CI-NEB approach to locate possible saddle points (transition states). Due to technical and computational difficulties in optimizing these large molecular interactions, we only have considered the adsorption of naphthalene and benzocoronene on the vacancy surface to address potential differences between small and large PAHs in the chemisorption process. For the PAH approaching the surface in parallel, the adsorption is studied for both naphthalene and benzocoronene. For a perpendicular orientation, we studied only naphthalene due to technical difficulties, see also image 1 shown in Fig. 5.9 and 5.10 respectively.

Parallel Adsorption. Fig. 5.9 shows the minimum energy path for the adsorption process of naphthalene and benzocoronene leading to the chemisorption of the carbon atoms, in para (opposite carbon sites of the hexagonal ring), forming C-Si and C-O bonds (image 8 in Fig. 5.9). Image 1 represents an optimized geometry of the PAH at a distance of about 5.6 Å from the surface. Image 8 is the optimized PAH chemisorbed on the vacancy which is the final product.

The adsorption process is barrierless and with large exoergic reaction energy of about -2.2 eV for naphthalene. We also reported the minimum energy path for benzocoronene (red curve in Fig. 5.9) to check how the path change for large surface area molecules. Benzocoronene also has large reaction energy of about -2.59 eV with a barrierless and exoergic adsorption. The benzocoronene images are lower in energy with respect to the naphthalene ones due to the larger dispersion energy with respect to naphthalene (see Table 5.4).

Perpendicular Adsorption. When the molecule is oriented perpendicularly with respect to the surface, as shown in image 1 in Fig. 5.10, the adsorption on the V_{MgO}-[010]-fo leads, during the optimization process, to the dissociation of C-H bond of the PAH. In contrast, this process on the pristine and transition metal surfaces does not lead to dissociation but only adsorption (see Fig. 5.4). On the vacancy, the optimized minimum energy path (Fig. 5.10), with the CI-NEB method, shows a barrierless and

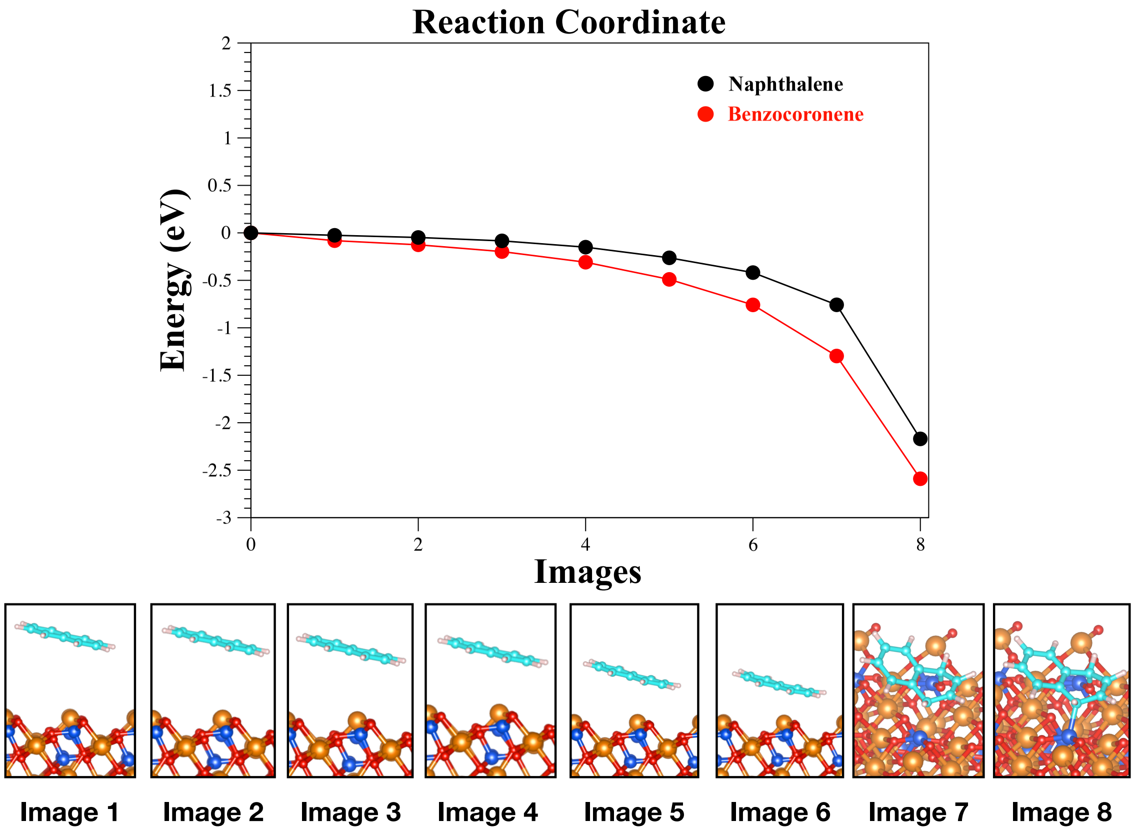

Figure 5.9: Optimized minimum energy path of the adsorption of naphthalene (black curve) and benzocoronene (red curve) on V_{MgO}-[010]-fo. The optimized geometry, only for naphthalene, of all images is reported below the plot. Image zero is the surface and the molecule at infinite distance.

exoergic reaction of -3.5 eV. Therefore, the dissociation (perpendicular adsorption) is more favorable than the adsorption (parallel adsorption) by about -1.3 eV.

The reagent (image 1) has been optimized perpendicularly and distant about 6.5 Å with respect to the vacancy surface. Along the reaction path, the molecule approaches the surface, chemisorbing a carbon atom on the undercoordinated Si atom on the vacancy (C-Si interaction). This results in a C-Si bond length of about 2.13 Å compared to typical C-Si bond length in silane species: 1.87 Å.[281] The electron donation of the C-Si interaction causes, at the same time, the transposition of the hydrogen to the neighbor oxygen atom on the vacancy forming an O-H bond with a distance of about 0.99 Å typical for hydroxyl groups.[281] The last step implies the adsorption of the remaining carbon skeleton on the surface, as shown in image 8 on Fig. 5.10.

The spin density isosurfaces show a large population of spin-down localized on the Si atoms and spin-up localized on the O atoms of the V_{MgO}-[010]-fo surface. The Voronoi charge analysis shows a partial positive charge on the Si atom (0.897) and a partial negative charge on the O atom (-0.625). After the dissociation, the partial electronic charge is reduced to 0.625 for the Si atoms, gaining electrons, and -0.356 for the O atom, donating electrons. The Voronoi charge analysis shows a donation of the electrons from the 2p orbital of the C atom of naphthalene to the 3p orbital of the undercoordinated Si atom on the vacancy, whereas the O atom donates electron density to the proton (H) dissociated from the PAH. This behavior is similar to the catalytic effect of "Frustrated Lewis Pairs" (FLPs) that are a Lewis acid and base that are not able to bind due to geometrical hindrance. Therefore, the geometrical hindrance causes the increase of the strength of the Lewis acid and base. The simultaneous electron transfer is responsible for the cleavage of the C-H bond through a barrierless reaction promoted by an O and undercoordinated Si atoms which is similar to the electron transfer mechanism of the FLPs.[282]

Table 5.5 reports the reaction energy (dissociation energy) for all PAHs on the V_{MgO}-[010]-fo based on the two studied mechanisms (perpendicular and parallel). For the parallel adsorption, naphthalene, anthracene, and fluoranthene show comparable reaction energies, whereas both coronene and pyrene show exoergic reaction energies larger by about -0.4 eV. The exoergicity of benzocoronene is even larger (-5.25 eV) with respect to all PAHs. Anthracene has slightly lower reaction energy with respect to naphthalene and fluoranthene. This might reflect the fact that the electron density is mainly localized in the central ring of anthracene. The electron density is lower in the terminal ring (the ring bound with the surface) than the central one.[39,124,283] However, on the vacancy surface, anthracene prefers to bind with the terminal ring, not with the central one, as the latter would require major structural changes. As a result, the reaction energy of anthracene is not as large as for naphthalene and fluoranthene. The reac-

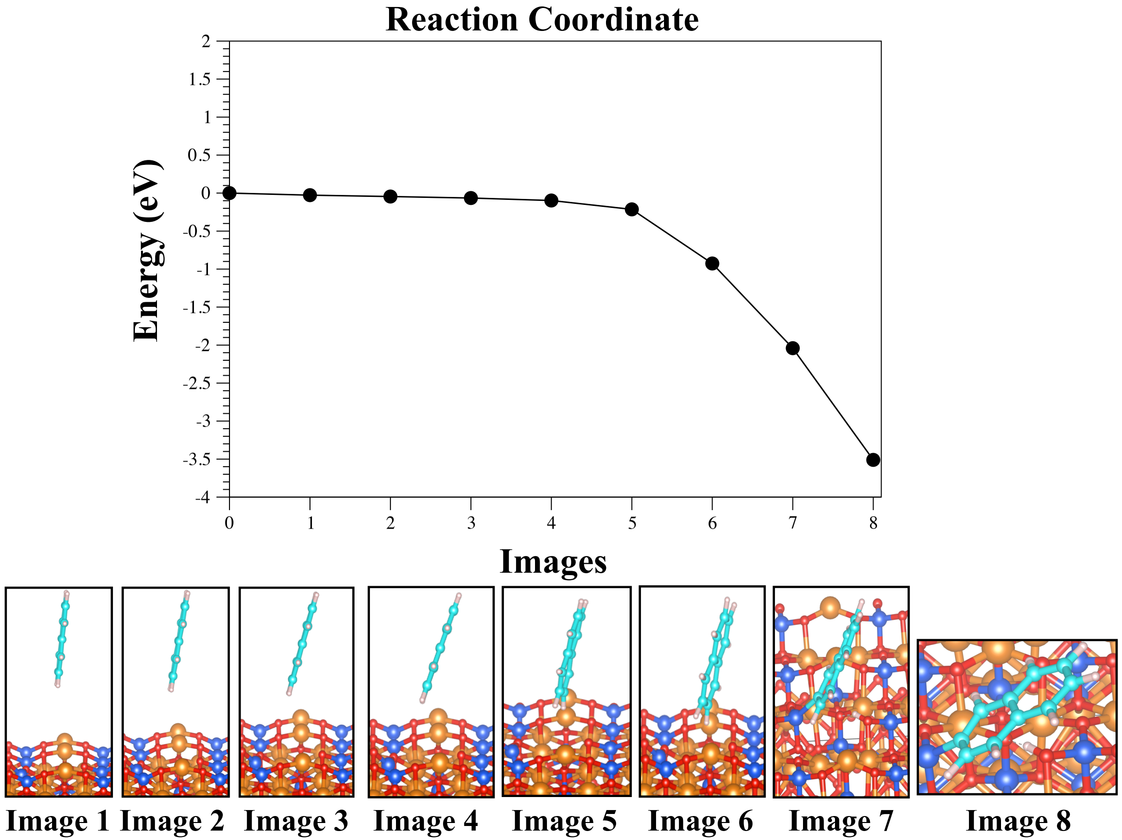

Figure 5.10: Optimized minimum energy path of the CH dissociation of naphthalene on V_{MgO}-[010]-fo. The optimized geometry of all images is reported below the plot. Image zero is the surface and the molecule at infinite distance.

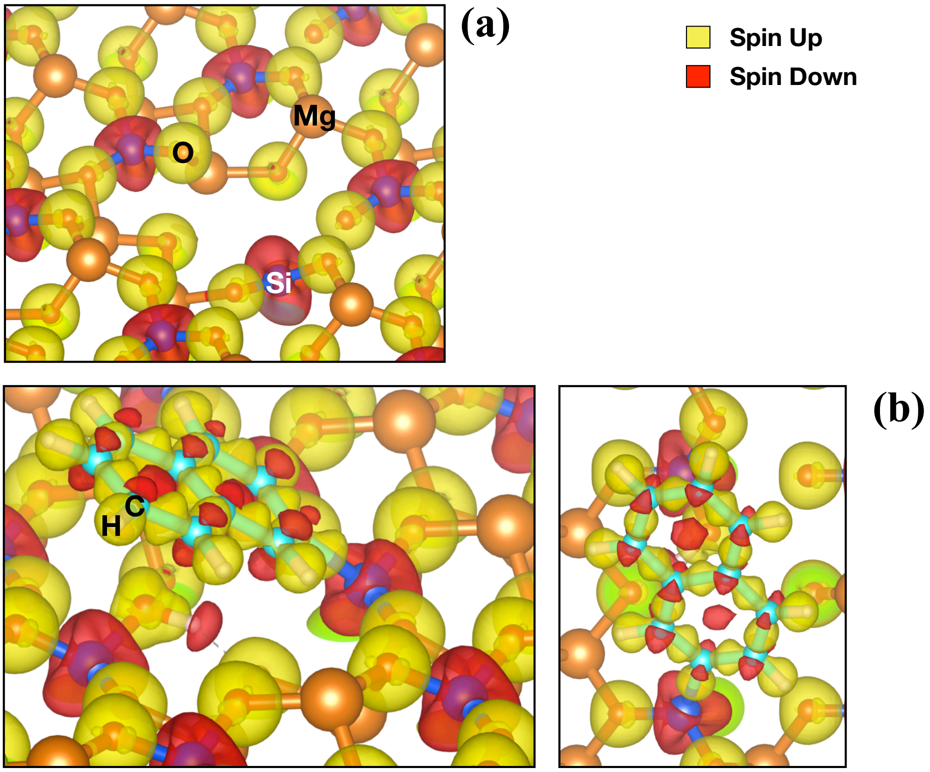

Figure 5.11: Spin density isosurface (isovalue 0.007 e/A^3) of V_{MgO}-[010]-fo (a) and the dissociation of the CH bond of naphthalene on the V_{MgO}-[010]-fo (b). Yellow density indicates spin up population and red density spin down one.

Table 5.5: Reaction energies for the adsorption of PAHs on V_{MgO}-[010]-fo through a perpendicular ($E^{\perp}_{react}$) and parallel ($E^{=}_{react}$) adsorption.

	$E^{\perp}_{react}$ (eV)	$E^{=}_{react}$ (eV)
Naphthalene	-3.51	-2.21
Antracene	-3.22	-2.76
Fluoranthene	-3.55	-2.10
Pyrene	-3.92	-1.23
Coronene	-3.92	-2.15
Benzocoronene	-5.25	-2.59

tion energy trend, for the perpendicular adsorption, is the reverse of the parallel adsorption in which anthracene is more stabilized with respect to naphthalene and fluoranthene due to the perfect geometrical fit with the vacancy surface (see discussion in Binding Energy Analysis section and Table 5.3)

The C-H dissociation trough a perpendicular adsorption mechanism is more energetically favourable and, therefore, more likely to happen with respect to the parallel adsorption (Table 5.5). Based on the Bell–Evans–Polanyi principle,[138,139] higher reaction energies are associated with low energy barriers and, therefore due to the large exoergicity, we would expect a barrierless process also for anthracene, fluoranthene, pyrene and coronene.

5.4. Astrochemical and Cosmochemical Implications

The study of the interaction of silicate minerals with PAHs in star forming regions is important since it may relate to the organic composition of comets and asteroids. The latter locks up a variety of organic molecules including the prebiotic building blocks of life as well as PAHs.[46] During the phase of the formation of a star, silicate dust grains surrounding the protostar coagulate to form planetesimals and cometesimals that eventually will lead to planet formation. Therefore, the cometary and asteroidal composition locks up valuable information about the processes that form molecules in space.[8,46]

In this study, we focused on crystalline forsterite as the main component of silicate grains, asteroids, and meteorites.[44,284] Silicate minerals in protoplanetary disks and the solar system often have a crystalline nature as revealed by observations of dust disks around young stellar objects, comets and asteroids.[35] In the ISM, silicates have strong infrared Si-O stretching mode and O-Si-O bending mode absorption features around 9.7 µm and 18 µm, respectively.[285] While IR observations reveal that interstellar silicate grains lack large scale order,[286] X-ray absorption studies reveal short scale crystalline structures.[287] Possibly, interstellar silicates are polycrystalline and, in that case, their adsorption behavior would be well described by the study presented here. However, in the ISM, there are no direct evidence of the presence of crystalline silicate and, thus, this issue is still under investigation.[44,286]

The composition of the dust, asteroids and meteorites (silicate materials) is largely dominated by silicate structures belonging to the olivine and pyroxene's families with stoichiometric formulae $Mg_{2x}Fe_{2-2x}SiO_4$ and $Mg_xFe_{1-x}SiO_3$, respectively. The composition of silicate materials in the universe is usually very rich in Mg and poor of Fe (Mg/Fe ratios less than a few percent).[288] The trace of transition metals is embedded in forsterite as point defects,[236] distortionary rearrangement of a perfect crystal lattice, along with Mg, Si, and MgO Schottky vacancy.[217,264] Point defects might already have formed in the envelope of AGB stars or may reflect energetic processing of silicate grains in the ISM by *e.g.*, cosmic rays,[289,290] whereas thermal annealing and irradiation by the stars are the processes taking place in protoplanetary disks.[291] Molecular dynamic simulations suggest the vacancy formation has been preferentially formed around the AGB stars through O-loss or Schottky defect creation.[264]

Part of the condensed dust in the ISM is formed by PAHs along with other aromatic carbonaceous molecules due to the formation of cluster agglomerates by the π-stacking of their aromatic skeleton.[32,292] In space, PAHs are important to maintain the energy and ionization balance in some regions of the interstellar medium as well as for the production of the most important molecule in the universe, H_2.[16,39] In carbonaceous meteorites, PAHs were hypothesized to be formed by the conversion of aliphatic compounds to aromatic ones through post-Fischer-Tropsch synthesis at low temperature catalyzed by minerals at 360-400 K. However, due to the large abundance of non-alkylated PAHs with temperatures between 400-800 K, the hypothesis of PAH formation post-Fischer-Tropsch synthesis was rejected.[50] Therefore, the origin of PAHs in asteroidal settings is still to be clarified, whereas it is clear that in circumstellar regions and the ISM are the most likely sources for the formation of these aromatic compounds.[44]

The silicates found in meteorites, specifically carbonaceous chondrites, have characteristic composition of non-volatile elements, *e.g.* Fe, Ni, Mg, etc., in which the abundance is comparable to the abundance of elements observed in the Sun.[293,294]

The abundance of PAHs in the Murchinson carbonaceous meteorite is about 1.82 mmol/g with a large abundance of PAHs with four aromatic units.[53] PAHs with more than six aromatic units such as coronene ($C_{24}H_{12}$) and benzocoronene ($C_{28}H_{14}$) have not yet been identified in meteorites. The presence of fullerene in meteorites is suspected and still need further clarifications.[295] Therefore, we considered studying the interaction of coronene and a similar molecule with an extra aromatic ring (benzocoronene) along with fullerene to clarify the matter about the reason why large organic species were not yet detected.

The potential catalytic activity of forsterite and its defective surfaces, revealed by this study, provides a new view on why large PAHs might not be present in carbonaceous meteorites. The degradation of PAHs, as we saw for the CH activation on the vacancy surface, is favorable for PAHs up to 7 aromatic units. In the ISM the barrier for H-loss from PAHs, such as coronene, in the gas phase is 4.7 eV,[183] and it can be easily promoted by energetic UV-photons (about 12 eV). Astronomical models imply that photodestruction is more rapid for small PAHs than for large PAHs.[41,296] In our calculations based on the binding and reaction energies, on a solid surface, we see the opposite trend and the dissociation rate is more favorable for large PAHs, suggesting that defects in crystalline olivine might catalyze the dissociation of the C-H bond of PAHs in an asteroidal setting. Therefore, this work provides the basis for future astronomical modeling and experimental studies. In particular, the dissociation sequence of each C-H bond of PAHs as well as the estimation of energy barriers for the pristine and metal-doped surfaces needs to be clarified in future works.

5.5. Conclusions

We employed periodic DFT-D4 to study the interaction of PAHs with the [010] forsterite surface and its defective surfaces: Fe, Ni-doped surfaces. Furthermore, we studied the catalytic property (CH activation) of the MgO Schottky vacancy. We studied the adsorption of naphthalene, anthracene, fluoranthene, pyrene, coronene, benzocoronene, and fullerene on these four [010] forsterite surfaces. With the exception of fullerene, all species adsorb on the surfaces maintaining angles and dihedral angles close to the gas-phase configuration. A large surface area allows large contact points (number of atomic interactions) with the surface. Excluding the vacancy surface, we found that all organic species, in this study, present larger binding energy on the Fe-[010]-fo surface with respect to Ni and pristine surface which is the opposite behavior of benzene-cation complexes in the gas-phase. These small differences in the binding energy for the adsorption of PAHs on pristine and transition metal surfaces are caused by differences in the number of contact points. The vacancy has shown different behavior with respect to pristine and transition metal surfaces due to the formation of a covalent bond with PAHs. Specifically, C-O and C-Si bonds. Anthracene has a larger binding energy with respect to other PAHs due to the formation of perfect $\widehat{OCC}$ and $\widehat{SiCC}$ angles of 109° and 120° characteristic of silane complexes. Deviation from these angles are reflected in the differences in binding energy of PAHs on the vacancy surface. Pyrene and coronene physisorb on the vacancy without covalent bond formation. For the case of coronene, the physisorption causes the reconstruction of Si-O bonds on the vacancy. Fullerene adsorption occurs through the formation of C-O and C-Si bonds on the 6-membered ring analogous to PAHs chemisorption. The larger binding energy of the chemisorption of fullerene on the vacancy reflects the formation of covalent bonds that break the icosahedral symmetry of the buckyball.

We found that based on the orientation of the molecule with respect to the vacancy surface the barrierless adsorption or the adsorption with a barrierless CH dissociation might take place on the surface; parallel and perpendicular to the surface, respectively. The perpendicular adsorption, with associated CH dissociation, is energetically more favorable than the parallel adsorption. Therefore, the vacancy has potential catalytic activity for the dissociation of CH bond of PAHs. For the CH dissociation process, the charge analysis has shown an electron donation of the O atoms to the C atoms and electron attraction of the H to the Si atom. This causes splitting of the C-H bond and the formation of C-Si and O-H bonds on the surface. This mechanism is similar to the electron transfer mechanism of Frustrated Lewis Pairs (FLPs) catalysts.

Hence, forsterite shows potential catalytic activity for the dissociation of aromatic CH which might be used as a cheap and safe catalyst. Furthermore, the catalytic potential of forsterite might shed light on the formation of the so-called organic inventory of star-forming regions in space. This study will follow up with future studies on addressing the selectivity of the vacancy for the dissociation of the hydrogen bound with different carbon sites of the PAHs as well as clarifying the catalytic activity of the pristine surfaces and how to release the fragmented PAH strongly bound with the catalytic site.

5.6. Appendix

Binding Energies

Table 5.6: Binding energies (E_{bind}) of the adsorption of PAHs and fullerene onto [010] forsterite surfaces.

	$E_{bind}^{[010]-fo}$ (eV)	$E_{bind}^{Fe-[010]-fo}$ (eV)	$E_{bind}^{Ni-[010]-fo}$ (eV)	$E_{bind}^{V_{MgO}-[010]-fo}$ (eV)
naphthalene	1.14[12]	1.46[12]	1.17[12]	2.21
anthracene	1.34	1.65	1.37	2.76
fluoranthene	1.57	1.97	1.26	2.1
pyrene	1.09	1.51	1.36	1.23
coronene	2.09	2.23	1.93	2.15
benzocoronene	2.32[12]	2.61[12]	2.4[12]	2.59
fullerene	1.56	1.62	1.31	3.51

Population Analysis

The electronic structure and the nature of chemical bonding are studied with the projected density of state (PDOS), the crystal orbital overlap (COOP), and hamilton population (COHP).[297] The theoretical level used for the PDOS, COOP, and COHP, consists of a PBE+U/TZP single-point calculation on the PBE/DZP optimized geometry (explained in detail in a previous work[12]).

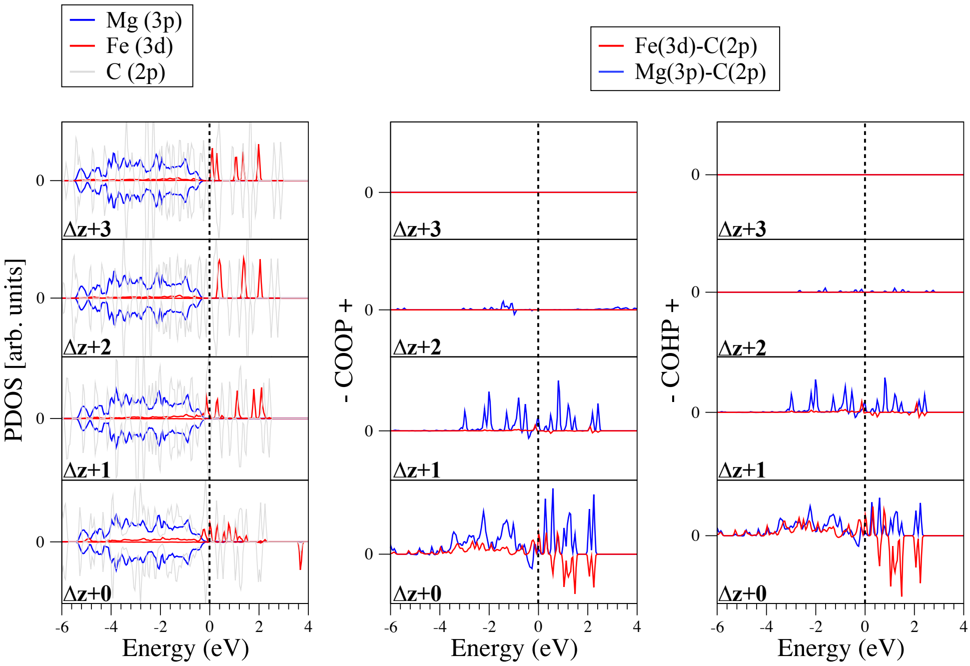

Figure 5.12: PDOS, COOP, and COHP of benzocoronene adsorbed on Fe-[010]-fo at different distances from the surface (Δz=+0 Å,+1 Å,+2 Å,+3 Å) with the respective atomic legend reported. For the PDOS, the peaks down and up refer to spin down and up, respectively. For the COOP and COHP, positive values are bonding contribution and negative ones are anti-bonding contribution. The Fermi level has been shifted at 0 eV.

The binding energy analysis provides meaningful insights into understanding the strength of the adsorption of the four forsterite surfaces. However, the only binding energy analysis does not provide information on the bonding nature between the molecule and the surface. Therefore, we calculated, as test-case, the PDOS, COOP, and COHP only for the adsorption of the PAH that has large binding energy when adsorbed on the forsterite surfaces: benzocoronene on Fe-[010]-fo and V_{MgO}-[010]-fo, for instance. We decided to consider the only benzocoronene in view of its large surface area (40.73 Å), and for the surface, we limit ourselves to Fe-[010]-fo and V_{MgO}-[010]-fo since those are the surfaces that show higher binding energy for most of the cases of this study. Specifically, we calculated the PDOS of benzocoronene at different distances from the surface (0, 1, 2 and 3 Å far from the surface). We reported only the valence band region since we are interested in shedding light on the binding nature of the molecular interaction with the surface. In Fig. 5.12, we report the PDOS for the benzocoronene adsorbed on the Fe-[010]-fo surface. The valence band is dominated by the electrons of the 2p orbitals of the O atoms, followed by the electrons of the 3p orbitals of the Mg atoms and 3d orbitals of the Fe atoms. When benzocoronene is interacting with the surface (Δz+0 Å), we notice an overcrowded region of small peaks belonging to orbitals of C and Fe that suggest orbital interaction. Once the molecule moves away from the surface the region of the Fermi level becomes less busy with larger gaps between the peaks of all three atoms reflecting the reduced interaction of the molecule with the surface.

The PDOS provides a good description of the electronic contribution of the atoms to the overall band structure, however, does not provide information about the bonding and antibonding nature of these electrons. Therefore, we partitioned the density of state in the bonding and antibonding contribution of the specific atoms (COOP spectra). Fig. 5.12 report the COOP spectra for the orbital interaction between Mg and C atoms as well as Fe and C atoms. The upward and downward peaks reflect bonding and anti-bonding contribution, respectively. Qualitatively, we see that the bonding contribution prevails with respect to the antibonding contribution. Once the molecule is 1 Å away from the surface (Δz+1 Å), the antibonding contribution disappears since the electron-electron repulsion is lower. Once the molecule is 2 and 3 Å away (Δz+2 Å and Δz+3 Å, respectively) from the surface there is not bonding contribution since the electronic interaction becomes weaker.

The COHP is the same as the COOP, but in this case, we partition the band energy rather than the electronic structure. Therefore, the COHP usually is the opposite of the COOP, but for simplicity, we inverted the sign of the peaks for ease of comparison to COOP. As expected, COHP has a similar trend with respect to COOP for the case of benzocoronene on Fe-[010]-fo, shown in Fig. 5.12.

For the interaction of benzocoronene with the V_{MgO}-[010]-fo, Fig. 5.13, the PDOS is dominated by the electron of the 2p orbitals of the O atoms followed by 3p orbitals of Mg, 3p orbitals of Si, in line with the PDOS bulk structure of forsterite,[12] and 2p orbitals of the C atoms. Due to the presence of three different types of interaction, it is difficult to analyze substantial variations in the PDOS at three different distances from the

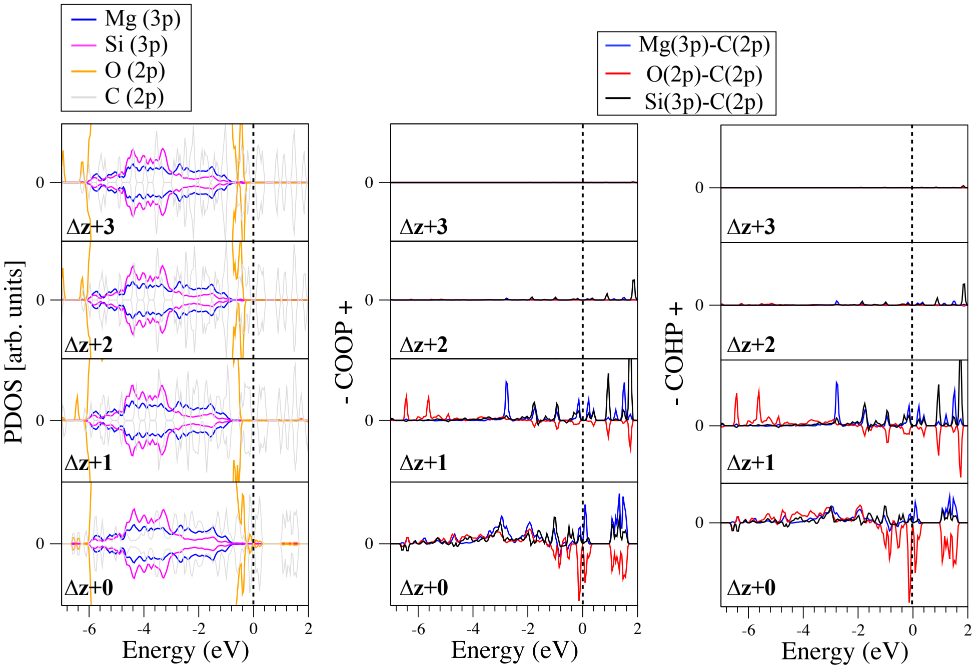

Figure 5.13: PDOS, COOP, and COHP of benzocoronene adsorbed on V_{MgO}-[010]-fo at different distances from the surface (Δz=+0 Å,+1 Å,+2 Å,+3 Å) with the respective atomic legend reported. For the PDOS, the peaks down and up refer to spin down and up, respectively. For the COOP and COHP, positive values are bonding contribution and negative ones are anti-bonding contribution. The Fermi level has been shifted at 0 eV.

surface. Instead, the COOP and COHP show non-bonding peaks as well as larger bonding peaks for the interaction of O-C orbitals. This suggests the presence of a covalent bond formation since the electron of the 2p orbitals of C atoms come close to the electrons of the 2p orbital of the O atoms repelling each other.

Geometrical Parameters

In the previous section (Population Analysis), we see that there is not orbital interaction when the molecule is 3 Å away from the surface. Therefore, we report the geometrical parameters considering only C-Mg and C-M (M is a transition metal) interactions with distances less than 3 Å.

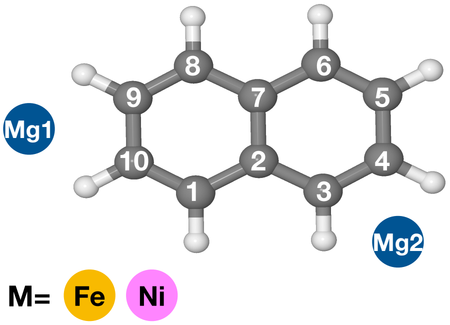

	[010]-fo	Fe-[010]-fo	Ni-[010]-fo	V_{MgO}-[010]-fo
Mg1-C9	2.73			
Mg1-C10	2.50			
Mg2-C2	2.80			
Mg2-C3	2.46	2.53		
Mg2-C4	2.59	2.50	2.44	
Mg2-C5			2.85	
M-C1		2.26	2.19	
M-C10		2.14	2.22	
M-C9		2.89	2.86	
Si-C8				1.98
O-C1				1.46
$\widehat{C4C3C2}$	120.42	120.55	119.92	120.85
$C\widehat{10C1C}2$	120.00	119.50	120.17	110.07
$\Theta(C4C3C2C1)$	173.06	179.33	179.81	-176.04
$\Theta(C10C1C2C3)$	179.30	164.75	-176.48	148.04

Figure 5.14: Schematic figure of naphthalene structure and its atomic labels interacting with Mg and transition metals atoms (Fe and Ni) on the surface. Table of bond distances (-) in Angstrom (Å), angles ($\widehat{}$) and dihedral angles (Θ), in degree (°), of the interaction of naphthalene with the [010] forsterite surfaces. The missing values indicate bond distances larger than 3 Å. The geometrical parameters of this molecule adsorbed on [010]-fo, Fe-[010]-fo, and Ni-[010]-fo are calculated from the optimized geometry of prior work.[12]

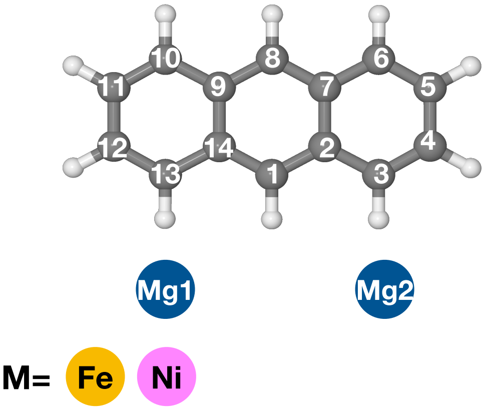

	[010]-fo	Fe-[010]-fo	Ni-[010]-fo	V_{MgO}-[010]-fo
Mg2-C2	2.63			
Mg2-C3	2.45			
Mg2-C4	2.64	2.81	2.93	
Mg2-C5				2.70
Mg1-C11		2.87	2.80	
Mg1-C12	2.75	2.43	2.46	
Mg1-C13	2.50			
Mg1-C14	2.94			
M-C14		2.65	2.58	
M-C1		2.14	2.15	
M-C2		2.42	2.51	
Si-C10				2.00
O-C13				1.46
$C12\widehat{C13}C14$	119.94	120.28	120.02	110.02
$C14\widehat{C1}C2$	121.15	121.17	121.25	121.17
$C2\widehat{C3}C4$	121.38	119.95	119.71	121.04
$\Theta(C12C13C14C1)$	-179.46	-178.41	176.72	150.19
$\Theta(C1C2C3C4)$	166.67	-174.89	-177.39	173.75

Figure 5.15: Schematic figure of anthracene structure and its atomic labels interacting with Mg and transition metals atoms (Fe and Ni) on the surface. Table of bond distances (-) in Angstrom (Å), angles ($\frown$) and dihedral angles (Θ), in degree (°), of the interaction of anthracene with the [010] forsterite surfaces. The missing values indicate bond distances larger than 3 Å.

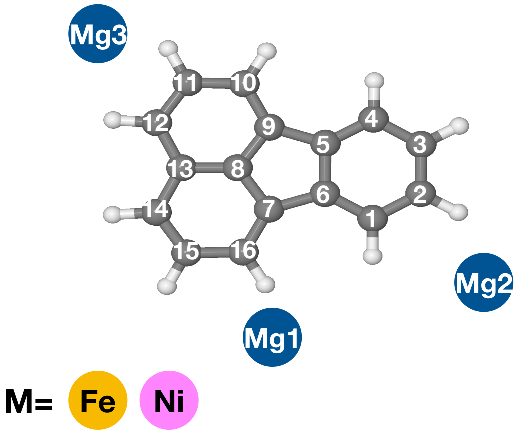

	[010]-fo	Fe-[010]-fo	Ni-[010]-fo	V_{MgO}-[010]-fo
Mg1-C16	2.41			
Mg1-C13				2.68
Mg1-C14				2.88
Mg1-C15	2.71			
Mg1-C7	2.71			
Mg2-C2	2.44	2.43	2.51	
Mg2-C1	2.91			
Mg2-C3	2.86	2.70	2.53	2.93
Mg3-C11	2.76	2.74		
M-C15		2.96		
M-C16		2.17		
M-C7		2.23	2.66	
M-C6		2.88		
M-C8			2.32	
M-C9			2.66	
M-C13			2.86	
Si-C1				2
O-C4				1.47
$C14\widehat{C15}C16$	122.13	122.99	122.78	123.06
$C16\widehat{C7}C6$	134.71	135.79	135.74	135.99
$C6\widehat{C1}C2$	118.24	118.46	118.58	110.57
$C14\widehat{C13}C12$	126.81	127.20	128.73	128.05
$C13\widehat{C8}C7$	124.80	124.21	124.26	125.03
$\Theta(C15C16C7C6)$	-169.04	175.58	-176.31	-179.59
$\Theta(C2C1C6C7)$	178.30	179.04	178.82	-153.39
$\Theta(C14C13C12C11)$	179.53	174.07	-176.44	178.13
$\Theta(C13C8C7C6)$	171.84	179.28	179.76	177.89

Figure 5.16: Schematic figure of fluoranthene structure and its atomic labels interacting with Mg and transition metals atoms (Fe and Ni) on the surface. Table of bond distances (-) in Angstrom (Å), angles ($\widehat{}$) and dihedral angles (Θ), in degree (°), of the interaction of fluoranthene with the [010] forsterite surfaces. The missing values indicate bond distances larger than 3 Å.

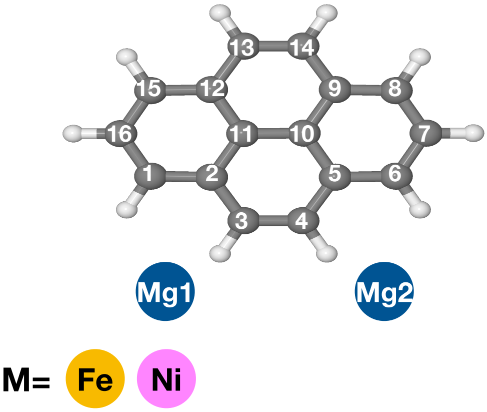

	[010]-fo	Fe-[010]-fo	Ni-[010]-fo	V_{MgO}-[010]-fo
Mg1-C2	2.70			
Mg1-C11	2.55			
Mg1-C12	2.99			
Mg2-C6	2.78	2.39	2.46	
Mg2-C7	2.61	2.91	2.70	
Mg2-C5		2.62	2.81	2.83
Mg2-C4				2.67
M-C16		2.97		
M-C1		2.22	2.40	
M-C2		2.30	2.17	
M-C3		2.96	2.67	
M-C11			2.78	
Si-C16				2.25
Si-C1				2.83
$\widehat{C1C2C3}$	120.34	121.98	122.01	120.91
$\widehat{C4C5C6}$	122.18	121.99	120.84	122.48
$C2\widehat{C11C}10$	119.84	119.59	119.73	120.23
$\Theta(C1C2C3C4)$	179.28	-172.83	-178.45	175.47
$\Theta(C4C5C6C7)$	178.38	175.94	176.18	176.01
$\Theta(C1C2C11C10)$	179.80	177.14	178.30	-169.24

Figure 5.17: Schematic figure of pyrene structure and its atomic labels interacting with Mg and transition metals atoms (Fe and Ni) on the surface. Table of bond distances (-) in Angstrom (Å), angles ($\frown$) and dihedral angles (Θ), in degree (°), of the interaction of pyrene with the [010] forsterite surfaces. The missing values indicate bond distances larger than 3 Å.

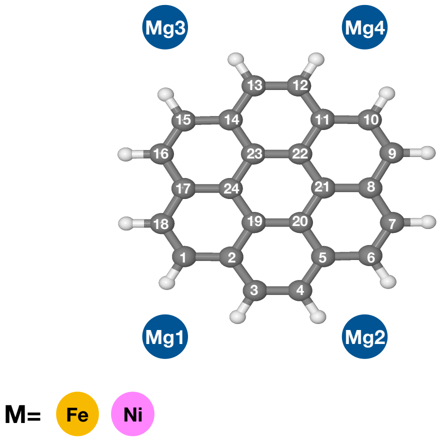

	[010]-fo	Fe-[010]-fo	Ni-[010]-fo	V_{MgO}-[010]-fo
Mg1-C1	2.57		2.50	2.59
Mg1-C2	2.80			
Mg1-C18			2.83	2.50
Mg2-C6	2.51	2.41		
Mg2-C5	2.63	2.81		
Mg2-C7		2.87		
Mg2-C4	2.99			
Mg4-C10	2.43	2.46		
Mg4-C11		2.69		
Mg4-C9	2.91			
Mg4-C12			2.52	2.40
Mg4-C13			2.69	2.54
Mg3-C11	2.77			2.90
Mg3-C15	2.93	2.60	2.88	
Mg3-C14	2.76	2.60		
Mg3-C13	2.83			
O-C3				2.28
M-C1		2.84		
M-C2		2.41		
M-C3		2.28		
M-C6			2.55	
M-C5			2.28	
M-C20			2.54	

Figure 5.18: Schematic figure of coronene structure and its atomic labels interacting with Mg and transition metals atoms (Fe and Ni) on the surface. Table of bond distances (-), in Angstrom (Å), for the interaction of coronene with the [010] forsterite surfaces. The missing values indicate bond distances larger than 3 Å.

	[010]-fo	Fe-[010]-fo	Ni-[010]-fo	V_{MgO}-[010]-fo
$\widehat{C18C1C2}$	120.61	120.89	121	121.47
$\widehat{C5C6C7}$	121.19	121.10	120.35	120.94
$\widehat{C9C10C11}$	121.00	120.99	121.05	120.50
$\widehat{C16C15C14}$	120.88	120.63	120.86	120.96
$\widehat{C18C17C16}$	121.87	121.90	121.70	121.88
$\widehat{C17C24C23}$	119.99	120.29	119.82	119.58
$\Theta(C18C1C2C3)$	178.05	-173.03	-177.82	179.96
$\Theta(C7C6C5C4)$	173.25	170.68	-175.06	-175.68
$\Theta(C9C10C11C12)$	-170.93	-174.64	-176.72	176.45
$\Theta(C16C15C14C13)$	176.15	-178.00	-179.91	-176.78
$\Theta(C17C24C13C22)$	-179.76	177.57	-179.98	174.68

Table 5.7: Table of angles ($\widehat{\ }$) and dihedral angles (Θ), in degree (°), of the interaction of coronene with the [010] forsterite surfaces. The atomic labels are referred to Fig. 5.18. The geometrical parameters of this molecule adsorbed on [010]-fo, Fe-[010]-fo, and Ni-[010]-fo are calculated from the optimized geometry of prior work.[12]

	[010]-fo	Fe-[010]-fo	Ni-[010]-fo	V_{MgO}-[010]-fo
$\widehat{C20C21C22}$	119.71	119.55	119.48	122.23
$\widehat{C6C5C4}$	120.91	120.80	120.58	121.35
$\widehat{C12C13C14}$	120.95	121	121	120.42
$\widehat{C17C16C15}$	120.88	120.51	120.66	120.77
$\Theta(C21C20C19C18)$	178.80	179.77	-179.28	-151.08
$\Theta(C17C16C15C14)$	174.51	-177.02	-178.34	165.39
$\Theta(C4C5C6C7)$	-175.56	-179.91	-179.92	-168.25
$\Theta(C20C19C18C17)$	-9.65	3.67	4.74	7.98
$\Theta(C1C2C3C4)$	3.87	-4.51	1.58	-1.51

Table 5.8: Table of angles ($\widehat{\ }$) and dihedral angles (Θ), in degree (°), of the interaction of benzocoronene with the [010] forsterite surfaces. The atomic labels are referred to Fig. 5.19.

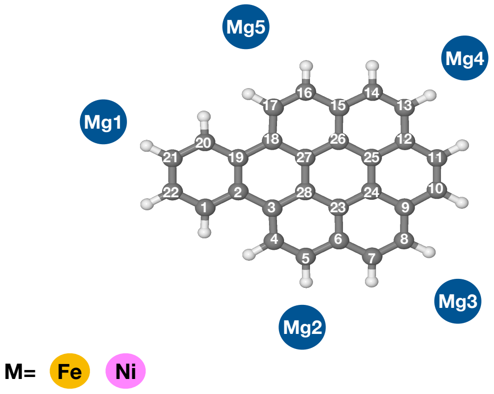

	[010]-fo	Fe-[010]-fo	Ni-[010]-fo	V_{MgO}-[010]-fo
Mg1-C21	2.59			
Mg1-C20	2.70			
Mg2-C5	2.50			
Mg2-C6	2.68			
Mg2-C22		2.70	2.74	
Mg3-C7		2.55	2.54	
Mg3-C8		2.53	2.55	
Mg3-C6		2.89	2.87	
Mg3-C24				2.67
Mg3-C25				2.61
Mg4-C13	2.54	2.50	2.51	
Mg4-C14		2.79	2.79	
Mg5-C15	2.91			
Mg5-C16	2.71	2.56	2.61	
Mg5-C17	2.62	2.76	2.73	
Mg5-C18	2.77			
Mg5-C15	2.91			
Mg5-C27	2.93			
M-C3		2.28	2.35	
M-C4		2.47	2.41	
M-C2		2.65	2.68	
Si-C20				2.02
O-C1				1.46

Figure 5.19: Schematic figure of benzocoronene structure and its atomic labels interacting with Mg and transition metals atoms (Fe and Ni) on the surface. Table of bond distances (-), in Angstrom (Å), for the interaction of benzocoronene with the [010] forsterite surfaces. The missing values indicate bond distances larger than 3 Å. The geometrical parameters of this molecule adsorbed on [010]-fo, Fe-[010]-fo, and Ni-[010]-fo are calculated from the optimized geometry of prior work.[12]

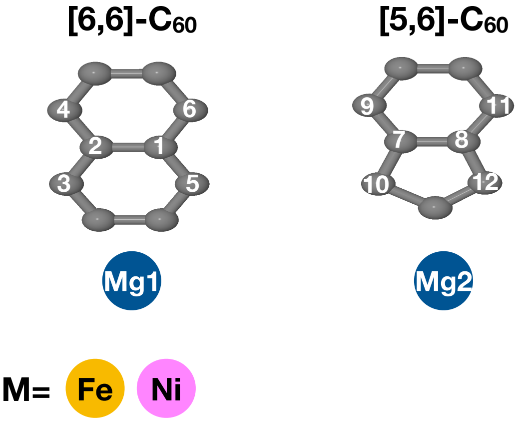

	[010]-fo	Fe-[010]-fo	Ni-[010]-fo	V$_{MgO}$-[010]-fo
Mg1-C1	2.56			
Mg1-C2	2.77			
Mg2-C7	2.77		2.81	2.90
Mg2-C8	2.88			2.59
Mg2-C11				2.93
M-C1		2.15	2.03	
M-C2		2.06	2.15	
Si-C5				1.99
O-C3				1.44
$\widehat{C9C7C10}$	118.81		119.62	123.23
$\widehat{C11C8C12}$	119.57			120.01
$\widehat{C4C2C3}$	108.23	107.32	107.62	110.02
$\widehat{C5C1C6}$	107.34	106.97	107.71	108.90
$\Theta(C10C7C8C11)$	140.12		143.19	153.27
$\Theta(C3C2C1C6)$	137.89	133.63		147.90

Figure 5.20: Schematic figure of fullerene [6,6] and [6,5] ring junctions and their atomic labels interacting with Mg and transition metals atoms (Fe and Ni) on the surface. Table of bond distances (-) in Angstrom (Å), angles ($\widehat{\ }$) and dihedral angles (Θ), in degree (°), of the interaction of fullerene with the [010] forsterite surfaces. The missing values indicate bond distances larger than 3 Å.